

Can the symmetric *Fermi* and eROSITA bubbles be produced by tilted jets?

Po-Hsun Tseng¹* H.-Y. Karen Yang^{2,3,4,5}† Hsi-Yu Schive^{1,5,6,7}‡ Tzihong Chiueh^{1,5,6}§

¹Institute of Astrophysics, National Taiwan University, Taipei 10617, Taiwan

²Institute of Astronomy, National Tsing Hua University, Hsinchu 30013, Taiwan

³Department of Physics, National Tsing Hua University, Hsinchu 30013, Taiwan

⁴Center for Informatics and Computation in Astronomy, National Tsing Hua University, Hsinchu 30013, Taiwan

⁵Physics Division, National Center for Theoretical Sciences, Taipei 10617, Taiwan

⁶Department of Physics, National Taiwan University, Taipei 10617, Taiwan

⁷Center for Theoretical Physics, National Taiwan University, Taipei 10617, Taiwan

2 July 2022

ABSTRACT

The *Fermi Gamma-Ray Space Telescope* reveals two large bubbles in the Galaxy, which extend nearly symmetrically $\sim 50^\circ$ above and below the Galactic center (GC). The recent discovery of giant eROSITA bubbles also shows such a symmetry about the GC, suggesting that they may originate from a single GC activity. Previous simulations of bubble formation that invoke active galactic nucleus (AGN) jets have assumed that the jets are vertical to the Galactic plane; however, in general there does not need to be a correlation between the jet orientation and the rotational axis of the Galactic disk. Using three-dimensional (3D) special relativistic hydrodynamic (SRHD) simulations that include cosmic rays (CRs) and thermal gas, we show that the dense clumpy gas within disk ISM disrupts jets collimation and confinement (“failed jets” hereafter), which in turn causes the failed jets to form hot bubbles. Subsequent buoyancy in the stratified atmosphere renders them vertical to form the symmetric *Fermi* and eROSITA bubbles (collectively, Galactic bubbles). Specifically, we find that (1) despite the relativistic jets emanated from the GC 12 Myr ago are at various angles $\leq 45^\circ$ with respect to the rotational axis of the Galaxy, the Galactic bubbles nonetheless appear aligned with the axis; (2) the edge of the eROSITA bubbles corresponds to a forward shock, driven by the hot bubble; (3) followed by the forward shock is a tangling contact discontinuity at the edge of the *Fermi* bubbles composed of turbulent and high-temperature (~ 2 keV) plasma in pressure balance with the external medium; (4) assuming a leptonic model we find that the observed gamma-ray bubbles and microwave haze can be reproduced with a best-fit CR power-law index of 2.4; (5) the 12 Myr time span between the present and the launch of short-lived jets appears to be the appropriate time scale for the observed GC Central Molecular Zone to form. The broad agreement between the simulated and the observed multi-wavelength features suggests that forming the Galactic bubbles by oblique AGN failed jets is a plausible scenario.

Key words: Relativistic hydrodynamics, *Fermi* bubbles, eROSITA bubbles, cosmic rays

1 INTRODUCTION

The detection of the *Fermi* bubbles (Su & Finkbeiner 2012; Ackermann et al. 2014; Narayanan & Slatyer 2017), two large bubbles symmetrically extending about 50 degrees above and below the Galactic plane, is one of the great discoveries of the *Fermi* Large Area Telescope (Atwood et al. 2009). The gamma-ray emission of the *Fermi* bubbles is observed in the energy range of $\sim 1\text{--}100$ GeV and has an almost spatially

uniform hard spectrum, sharp edges and an approximately flat brightness distribution (see Yang et al. 2018 for a review). Recently, the newly launched eROSITA (Predehl et al. 2021) conducted an all-sky X-ray survey with high-spatial resolution and revealed two gigantic bubbles (eROSITA bubbles hereafter) extending to ~ 80 degrees in Galactic latitudes, corresponding to an intrinsic size of 14 kpc across (Predehl et al. 2020). The remarkable resemblance between the eROSITA and *Fermi* bubbles suggest that they likely share the same origin (Yang et al. 2022). Their symmetry about the GC further suggests that these Galactic bubbles may be generated by powerful energy injections from the GC, possibly related to nuclear star formation (Crocker & Aha-

* zengbs@gmail.com

† hyang@phys.nthu.edu.tw

‡ hyschive@phys.ntu.edu.tw

§ chiuehth@phys.ntu.edu.tw

ronian 2011; Carretti et al. 2013; Crocker et al. 2015; Sarkar et al. 2015) or past AGN activity (Guo & Mathews 2012; Guo et al. 2012; Yang et al. 2012, 2013; Mou et al. 2014; Yang & Ruszkowski 2017). The latter scenario is what we will focus on in this work.

Previous attempts (Guo & Mathews 2012; Yang et al. 2012; Zhang & Guo 2020) to model the formation of the symmetric Galactic bubbles by AGN jets have typically assumed that the jets are vertical to the Galactic plane. While there are some observational indications of pc-scale jets from Sgr A* that are found to be perpendicular to the Galactic plane (Li et al. 2013; Zhu et al. 2019), generally speaking, the AGN jet orientation is determined by the black hole spin and the accretion disk in the black-hole vicinity and does not need to align with the rotational axis of the host galaxy. Indeed, observationally there is a lack of evidence for the alignment between AGN jets and the disk normal (e.g., Gallimore et al. 2006). The jets are often oblique to the disk normal (e.g. NGC 3079, Cecil et al. 2001; NGC 1052, Dopita et al. 2015), and there are even cases in which the jets lie in the plane of the disk (e.g. IC 5063, Morganti et al. 2015).

To this end, the aim of this work is to remove the assumption on jet orientations in the AGN jet models by introducing a dense, thin ISM disk that can interact with the central oblique jet, in an attempt to resolve the symmetry problem of the Galactic bubbles. More specifically, we use 3D SRHD simulations involving CR jet injections from the central supermassive black hole (SMBH) in the Galaxy to investigate whether the *oblique* jet scenario is able to produce the *symmetric* Galactic bubbles. We will verify whether the oblique jet model is consistent with the observed features of the Galactic bubbles, including the shape, surface brightness, and spectra of the *Fermi* bubbles (Ackermann et al. 2014) and microwave haze (Dobler & Finkbeiner 2008; Ade et al. 2013).

This paper is organized as follows. In Section 2, we describe the numerical techniques and initial conditions employed. In Section 3, we first present characteristics of our simulated Galactic bubbles, and then discuss how the disk affects the formation of the bubbles. We compare the morphology and profiles of the simulated eROSITA bubbles with the observed X-ray map in Section 3.2, and present the simulated and observed multi-wavelength spectra of the *Fermi* bubbles and microwave haze in Section 3.3. Finally, the summary and implications of our findings are given in Section 5.

2 METHODOLOGY

We use the GPU-accelerated SRHD adaptive-mesh-refinement (AMR) code GAMER-SR developed at the National Taiwan University (Schive et al. 2010, 2018; Tseng et al. 2021) to carry out the simulations of the Galactic bubbles formed by CR and relativistic-fluid injections from the GC.

The governing equations solving the special relativistic ideal fluid including CR advection, and dynamical coupling between the thermal gas and CRs without CR diffusion can be written in a succinct form as

$$\partial_t D + \partial_j (DU^j/\gamma) = 0, \quad (1a)$$

$$\partial_t M^i + \partial_j (M^i U^j/\gamma + p_{\text{total}} \delta^{ij}) = -\rho \partial_i \Phi, \quad (1b)$$

$$\partial_t \tilde{E} + \partial_j [(\tilde{E} + p_{\text{gas}}) U^j/\gamma] = 0, \quad (1c)$$

$$\partial_t (\gamma e_{\text{cr}}) + \partial_j (e_{\text{cr}} U^j) = -p_{\text{cr}} \partial_j U^j, \quad (1d)$$

$$\partial_i \partial^i \Phi = 4\pi G \rho, \quad (1e)$$

where the five conserved quantities of gas D , M^i , and \tilde{E} are the mass density, the momentum densities, and the reduced energy density, respectively. The reduced energy density is defined by subtracting the rest mass energy density of gas from the total energy density of gas. γ and U^j are the temporal and spatial component of four-velocity of gas. ρ is the gas density in the local rest frame defined by D/γ . p_{gas} is the gas pressure. p_{cr} and e_{cr} are the CR pressure and CR energy density measured in the local rest frame. p_{total} is the sum of p_{gas} and p_{cr} . Note that we simply replace p_{total} by p_{gas} in this paper as we have assumed $p_{\text{cr}} \ll p_{\text{gas}}$. Φ is a gravitational potential, and G is the gravitational constant. c is the speed of light, and δ^{ij} is the Kronecker delta notation. Throughout this paper, Latin indices run from 1 to 3, except when stated otherwise. The set of Eq. 1 is closed by using the Taub-Mathews equation of state (EoS; Taub 1948; Mathews 1971) that approximates the exact EoS (Synge 1957) for ultra-relativistically hot gases coexisting with non-relativistically cold gases.

GAMER-SR adopts a new SRHD solver (Tseng et al. 2021), which significantly reduce numerical errors in non- and ultra-relativistic limits caused by catastrophic cancellations in the conversion between primitive (ρ, U^j, p) and conserved variables (D, M^j, \tilde{E}) . GAMER-SR also adaptively and locally reduce the min-mod coefficient (Tseng et al. 2021) within the failed patch group rarely occurring in the SRHD solver, new patches allocations, and ghost-zone interpolations. In this manner, we provide an elegant approach to avoid the use of pressure/density floor, being unnatural but widely used in almost publicly available codes.

In order to track the evolution of CRs injected by the AGN jets and make predictions of the non-thermal radiation they produce, we adopt the CR hydrodynamic formalism and model the CRs as a second fluid (Zweibel 2013). The approach is similar to previous works of Guo & Mathews (2012) and Yang et al. (2012), but generalized to CRs that couple with thermal gas moving with relativistic speeds. The detailed implementations in GAMER-SR and tests of the algorithm can be found in a forthcoming paper (Chen et al. in prep.). In this approach, the CRs are treated as a single species without distinctions between CR electrons and protons, and the CR energy density e_{cr} is evolved according to Eq. 1e. The CRs are advected with the thermal gas and can have adiabatic compression and expansion with the gas. Also, we do not simulate the spectral evolution of the CRs and assume that the CR-to-gas pressure ratio is much less than 1 so that the contribution of CR pressure gradient to the momentum of the gas can be ignored (we will see that the ratio is around 0.1–0.2 throughout the simulations). Therefore, in the simulations we have neglected the cooling of CRs because it should have a negligible impact on the overall dynamics.

As stressed by Yang et al. (2012), CR diffusion with a canonical diffusion coefficient of $\kappa \sim 3 \times 10^{28} \text{ cm}^2 \text{ s}^{-1}$ in

the Galaxy has a minor effect on the overall morphology of the *Fermi* bubbles as it only acts to smooth the CR distributions on the scales of $l \sim \sqrt{\kappa t} \sim 0.3$ ($t/1\text{Myr}$) kpc. Including anisotropic CR diffusion can also help to sharpen the edges of the bubbles due to interplay between the magnetic field and anisotropic CR diffusion with suppressed perpendicular diffusion across the bubble surface. As for the magnetic field, Yang et al. (2013) has found that the magnetic field within the *Fermi* bubbles needs to be amplified to comparable values to the ambient field in order to reproduce the microwave haze emission. We thus directly adopt the exponential model for the magnetic field distribution in our calculation for the haze (see descriptions in Section 2.1). For the above reasons, we have ignored CR diffusion and the magnetic field in the simulations.

2.1 The Galactic and Disk Models

As a proof-of-concept study, we approximate conventionally axisymmetric stellar potential of Milky Way by a plane-parallel potential that is symmetric about the Galactic plane, $z = 0$, in a simulation domain of $14 \times 14 \times 28$ kpc, slightly larger than the size of eROISTA bubbles. The plane-parallel potential is fixed throughout our simulations and given by

$$\Phi_{\text{total}}(z) = \Phi_{\text{bulge}}(z) + \Phi_{\text{halo}}(z), \quad (2)$$

where

$$\Phi_{\text{bulge}}(z) = 2\sigma_{\text{bulge}}^2 \ln \cosh \left(z \sqrt{\frac{2\pi G \rho_{\text{bulge}}^{\text{peak}}}{\sigma_{\text{bulge}}^2}} \right) \quad (3)$$

is the potential of an isothermal slab mainly contributed by stars around the Galactic bulge, and $\Phi_{\text{halo}}(z) = v_{\text{halo}}^2 \ln(z^2 + d_{\text{h}}^2)$ is a plane-parallel logarithmic dark halo potential.

With the isothermal assumption and the condition of hydrostatic equilibrium within the total potential of the disk and halo, as well as pressure equilibrium between the isothermal disk and the halo gas, we can write down the steady-state gaseous density distribution as

$$\rho_{\text{isoDisk}}(z) = \rho_{\text{isoDisk}}^{\text{peak}} \exp \left[-\frac{\Phi_{\text{total}}(z)}{k_B T_{\text{isoDisk}}/m_p} \right] \quad (4a)$$

, if $|z| < z_0$,

$$\rho_{\text{atmp}}(z) = \rho_{\text{atmp}}^{\text{peak}} \exp \left[-\frac{\Phi_{\text{total}}(z)}{k_B T_{\text{atmp}}/m_p} \right] \quad (4b)$$

, otherwise,

where m_p is the proton mass, T_{isoDisk} and T_{atmp} are the temperature of the isothermal disk and the ambient atmosphere, and $\rho_{\text{isoDisk}}^{\text{peak}}$ and $\rho_{\text{atmp}}^{\text{peak}}$ are the peak density of the disk and the atmosphere at $z = 0$, respectively.

We tabulate parameters adopted for the Galactic model in Table 1, except for $\rho_{\text{atmp}}^{\text{peak}}$ that can be derived from the other known parameters and the pressure equilibrium condition at the interfaces ($z = \pm z_0$) between the disk and the atmosphere. The density profile of Eq. 4 is shown in Fig. 1. Beyond the core radius (~ 2 kpc) the gas density decreases rapidly as a power-law.

To compute the predicted synchrotron radiation as a function of position, we adopt the default exponential magnetic

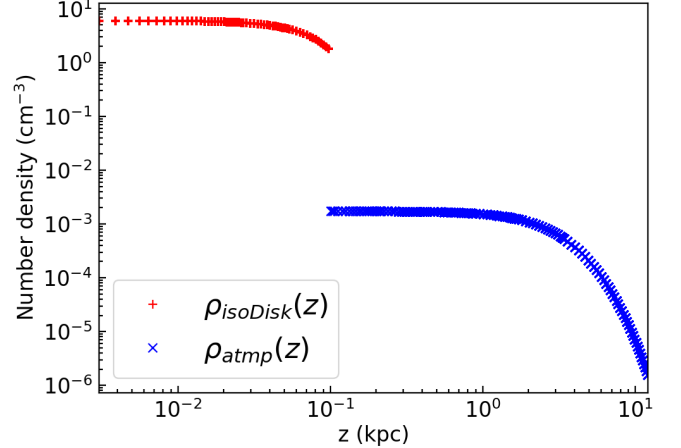


Figure 1. The density profile of the isothermal disk (red pluses) and the ambient atmosphere (blue crosses) along the positive z -axis. The density distribution is derived from the condition of hydrostatic equilibrium. The gas at the interface between the isothermal disk and the atmosphere at $z = 0.1$ is in pressure equilibrium.

field in GALPROP (Strong et al. 2007) that obeys the following spatial dependence:

$$|\mathbf{B}(R, z)| = B_0 \exp \left[-\frac{z}{z_0} \right] \exp \left[-\frac{R}{R_0} \right], \quad (5)$$

where $R = \sqrt{x^2 + y^2}$, B_0 is the average field strength at the GC, and z_0 and R_0 are the characteristic scales in the vertical and radial directions, respectively. We adopt $z_0 = 2$ kpc and $R_0 = 10$ kpc, which are best-fitting values in the GALPROP model to reproduce the observed large-scale 408 MHz synchrotron radiation in the Galaxy. We choose $B_0 = 50$ μG based on the observed field strength at the GC (Crocker et al. 2010).

2.2 The Clumpy Multiphase Interstellar Medium

A crucial component in our work is the clumpy ISM disk initialized by the publicly available pyFC code¹. pyFC randomly generates dimensionless 3D scalar field $f(\mathbf{x})$ that obeys the log-normal probability distribution with mean μ and dispersion σ , and follows the power-law Kolmogorov spectrum

$$D(\mathbf{k}) = \int k^2 \hat{f}(\mathbf{k}) \hat{f}^*(\mathbf{k}) d\Omega \propto k^{-\delta}, \quad (6)$$

where $\hat{f}(\mathbf{k})$ is the Fourier transform of $f(\mathbf{x})$. The spectrum $D(\mathbf{k})$ in the Fourier space is characterized by a power-law index $\delta = 5/3$, a Nyquist limit k_{max} , and a lower cutoff wave number k_{min} . k_{max} is one-half of the spatial resolution within the disk, and k_{min} is 375.0, corresponding to the maximum size of an individual clump of ~ 20 pc. Lewis & Austin (2002) and Wagner et al. (2012) have outlined a detailed procedure for constructing a clumpy scalar field, and we refer the readers for more information.

The density of the clumpy disk can then be obtained by taking the scalar products of $f(\mathbf{x})$ with $\rho_{\text{isoDisk}}(z)$ over all

¹ <https://pypi.python.org/pypi/pyFC>

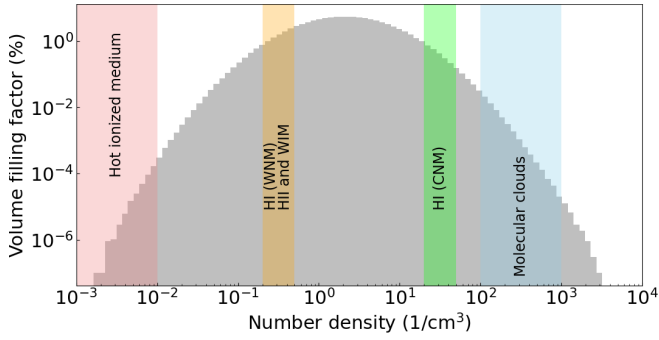


Figure 2. The volume filling factor as a function of initial number density within the disk without the jet source. The vertical bands from left to right depict the allowable number densities (Ferrière 2001) for hot ionized, warm neutral (WNM), warm ionized (WIM), cold neutral media (CNM), and molecular clouds.

cells within the disk, i.e., $\rho_{\text{ismDisk}}(\mathbf{x}) = f(\mathbf{x})\rho_{\text{isoDisk}}(z)$. Also, the thermal pressure equilibrium within the clumpy disk implies that the temperature of the disk is $T_{\text{ismDisk}}(\mathbf{x}) = T_{\text{isoDisk}}(z)\rho_{\text{isoDisk}}(z)/\rho_{\text{ismDisk}}(\mathbf{x})$. The last category in Table 1 summarizes the parameters of the clumpy disk and their references.

On the basis of this setup, we cover the AMR base level with $16 \times 16 \times 32$ root cells, refined progressively on the mid-plane at $z = 0$ based on the gradient of density. We also restrict the refinement level at 7 within the disk so that a molecular cloud can be adequately resolved by approximately 30 cells along their diameter of 20 pc. We plot the volume filling factor as a function of initial number density within the disk without the jet source in Fig. 2, and show a close-up view of the pressure, temperature, and number density slices in the $y - z$ plane through the center of the disk in Fig. 3.

2.3 Oblique jets

We simulate the jets emanating from the GC with an inclination angle 45° with respect to the Galactic plane in order to alleviate the constraint that the jet direction must be perpendicular to the Galactic plane, and in particular to investigate how the dense disk affects the bubble formation.

We use the following quantities to characterize the jets: the density contrast between the thermal gas contained in the jet source and the ambient gas, $\rho_{\text{jet}}/\rho_{\text{amb}} = 10^{-3}$, the temperature contrast, $T_{\text{jet}}/T_{\text{amb}} = 2 \times 10^4$, the CR-to-gas pressure ratio of 0.18, and the flow 4-velocity ($\beta\gamma = 0.6$) inside the jet source along the jet axis. The jet power is thus 3.2×10^{42} erg s $^{-1}$, resulting in an Eddington ratio of 0.008. Note that since we inject the jets at the center of the clumpy disk, we define the atmosphere gas density by the peak density of the isothermal disk on the mid-plane $z = 0$ (i.e. $\rho_{\text{isoDisk}}^{\text{peak}}$), as opposed to the *clumpy* density around the jet source.

The bipolar jets are constantly ejected from a cylindrical source starting from the beginning of simulation ($t = 0$) and suddenly quenched at $t = 1.2$ Myr before fully breaking out the disk. Without quenching, the Galactic bubbles at the present time would be asymmetric about the Galactic plane. The jet duration allows the total ejected energy to be 1.2×10^{56} erg, within the range of enclosed energy estimated by Predehl et al. (2020) between 8×10^{55} erg and 1.3×10^{56} erg.

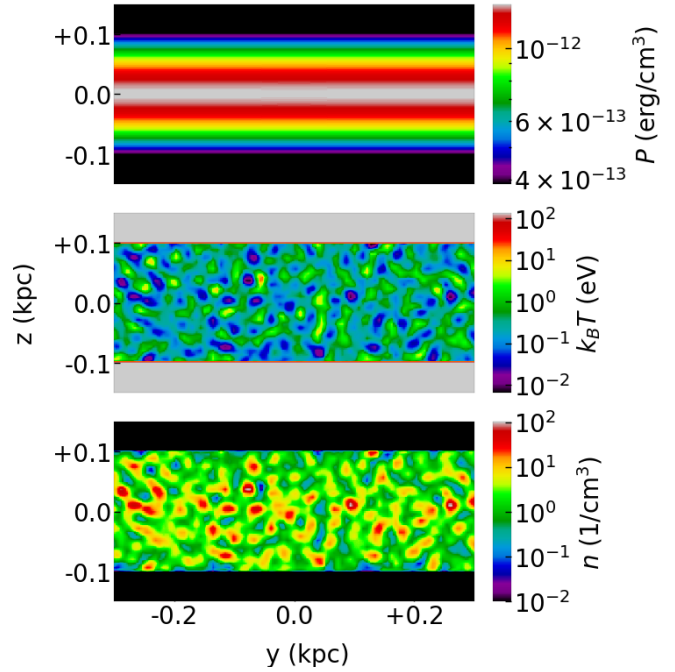


Figure 3. Close-up view of the initial pressure (top), temperature (middle), and number density (bottom) slices in the $y - z$ plane through the center of the disk.

The diameter and height of cylindrical source are 4 pc, leading to a source volume (~ 50 pc 3) much smaller than that of an individual clump by a factor of ~ 83 . By intentionally reducing the volume ratio of the jet source to an individual clump, we can mitigate the effect of the randomness of the clumps on the bubbles. Moreover, we resolve the jet source with the highest refinement level of 11, bringing the finest spatial resolution up to 0.4 pc.

3 RESULTS

3.1 Morphology and properties of Galactic bubbles

Fig. 4 shows the slices of pressure (top), temperature (middle), and number density (bottom) at the end of simulation $t = 12.39$ Myr. The slices pass through the bipolar jet source injecting along $z = -y$ direction.

The fiducial run (Fig. 4a) with the initial condition specified in Section 2 shows that the edge of the outermost bubbles is a forward shock, expanding to 12.5 kpc above and below the Galactic plane, with a semiminor axis about 6.8 kpc on the plane. The overall extent of the outermost bubbles is comparable to the two spherical objects of a radius of 6-7 kpc estimated by Predehl et al. (2020) for modeling the eROSITA bubbles. The temperature profile (left middle panel in Fig. 5) along the positive z -axis in Fig. 4 indicates that the temperature of the smooth region (purple band in Fig. 5) is around 0.3-0.5 keV, similar to 0.3 keV observed by Miller & Bregman (2016) and Kataoka et al. (2018a).

Followed by the forward shock is a turbulent and hot plasma extending to a height of ~ 8 kpc (Fig. 5). The extent of the turbulent plasma approximately agrees with that of the observed *Fermi* bubbles (Su et al. 2010). Also, the temperature of the plasma is around 2 keV, comparable to few

Table 1. Parameters of the disk, atmosphere, and gravitational potential in the simulations.

Parameter	Description	Value	Reference
Static stellar potential			
σ_{bulge}	Velocity dispersion of bulge	100 km s ⁻¹	(Valenti et al. 2018)
$\rho_{\text{bulge}}^{\text{peak}}$	Peak average density of bulge	4×10^{-24} g cm ⁻³	N/A
Static dark halo potential			
v_{halo}	Characteristic velocity	131.5 km s ⁻¹	(Johnston et al. 1995)
d_h	Core radius	12 kpc	"
Atmosphere			
T_{atmp}	Temperature of atmosphere	10 ⁶ K	(Tepper-García et al. 2015)
Isothermal disk			
z_0	Scale height of disk	100 pc	(Ferrière 2001)
$T_{\text{isoDisk}}^{\text{peak}}$	Temperature of disk	10 ³ K	"
$\rho_{\text{isoDisk}}^{\text{peak}}$	Peak density of disk	10^{-23} g cm ⁻³	"
Clumpy disk			
k_{\min}^{\dagger}	Cutoff wave number	375.0	(Ferrière 2001)
μ	Mean of scalar field	1.0	N/A
σ^{\ddagger}	Dispersion of scalar field	5.0	(Federrath et al. 2010)
δ	Power law index	-5/3	N/A

† $k_{\min} = 375.0$ leads to the size of an individual molecular cloud of ~ 100 pc.

‡ In numerical simulations of turbulence, Federrath et al. (2010) find $\sigma \sim 3.6$ and 35 for solenoidal (divergence-free) and compressive (curl-free) driving force, respectively, so that our adopted value of 5 is closer to their solenoidal result.

keV inside the *Fermi* bubbles estimated by observing X-ray absorption lines through the hot gaseous halo along many different sight lines in the sky (Miller & Bregman 2013). We also note that the turbulent, hot plasma is in pressure balance with the external medium, suggesting the outer edge of the *Fermi* bubbles is a contact discontinuity rather than a shock (Zhang & Guo 2020).

An interesting feature found in our simulations is that there are a pair of innermost bubbles (dashed box in the top panel of Fig. 4a) extending out from the GC on either side of the thin disk. The innermost bubbles are cold (1–10 eV), dense (10^{-4} – 10^{-2} cm⁻³), and underpressured with respect to the turbulent plasma but probably not related to the X-ray chimneys (Ponti et al. 2019) and radio bubbles (Heywood et al. 2019) due to their enormous difference in length (the total major-axis length of the X-ray chimneys and radio bubbles is 320 pc and 430 pc, respectively; however, the innermost bubbles is up to 4 kpc in length). The close-up view (right column in Fig. 5) of the vertical profiles and slices (Fig. 6) demonstrate that there is a sharp pressure jump at the edge of the innermost bubbles at $z = 3.62$ kpc, indicating that the innermost bubbles are an expanding reverse shock. The high-density upstream of the reverse shock requires an even higher density downstream. Continuing outward, there exists a dense shell before the gas density drops to values further downstream. The turbulent plasma is therefore bracketed between the downstream of reverse shock and of the outermost forward shock, thus heating the turbulent plasma up considerably.

We stress that either the outermost shock, turbulent plasma, or innermost bubbles are symmetric about the Galactic plane despite that the jets are tilted to the disk normal at an angle of 45°.

In addition to the fiducial run, in Fig. 4 we also show the slices of various gas properties at $t = 12.39$ Myr in different

Galactic environments. We compare the clumpy disk (Fig. 4a) with the smooth disk in a stratified atmosphere (Fig. 4b; the initial density profile is shown in Fig. 1). The results show that the clumpiness of the dense disk has an insignificant effect on the overall dynamics of bubbles. However, the outermost bubbles arising from the smooth disk in a uniform atmosphere (Fig. 4c) is quasi-spherical, suggesting that the stratification facilitates the elongation of the outermost bubbles significantly. Fig. 4c and 4d reveal that the development of the innermost bubbles is always associated with the disk. Also, without the disk (Fig. 4d), the outermost bubbles and the turbulent plasma would be oblique, indicating that the dense disk is crucial for the production of symmetric Galactic bubbles.

3.2 Morphology and Profiles in X-ray

The X-ray emissivity is computed for each computational cell using the MEKAL model (Mewe et al. 1985; Kaastra & Mewe 1993; Liedahl et al. 1995) implemented in the utility XSPEC (Arnaud 1996), assuming solar metallicity. The X-ray intensity map is then generated by projecting the emissivities along lines of sight pointing away from the solar position at $(R_{\odot}, 0, 0) = (8, 0, 0)$ kpc with angular resolutions of 0.5 degrees, where R_{\odot} is the Sun–GC distance.

We point out that the projections used throughout this paper are ‘perspective’, which has the effect of making a distant object appear smaller than the same object in a closer distance, in order to facilitate a reliable interpretation of simulated all-sky map. Also, the observed X-ray emission is contributed by all the gas in the Milky Way halo, which likely extends to a radius of ~ 250 kpc (Blitz & Robishaw 2000; Greco & Putman 2009), much bigger than our simulation box. Therefore, we first compute the X-ray emissivity from the simulated gas within a radius of 25 kpc away from the

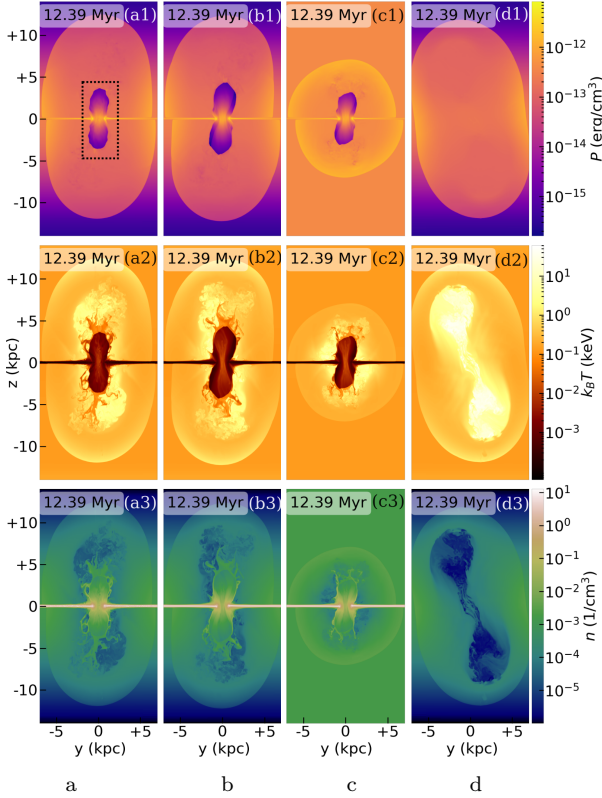


Figure 4. The slices of pressure (top), temperature (middle), and number density (bottom) at the end of simulation $t = 12.39$ Myr. The slices pass through a bipolar jet source injecting along $z = -y$ direction for a duration $t = 0\text{--}1.2$ Myr. Comparison between the clumpy (Fig. 4a) and the smooth disks (Fig. 4b) in a stratified atmosphere shows that the initial density distribution of the dense disk has an insignificant effect on the overall dynamics of bubbles. However, the outermost bubbles arising from the smooth disk in a uniform atmosphere (Fig. 4c) are nearly spherical, suggesting that the stratification facilitates the elongation of the outermost bubbles significantly. Fig. 4c and 4d reveal that the development of the innermost bubbles is always associated with the disk. Also, without the disk (Fig. 4d), the outermost bubbles and the turbulent plasma would be oblique, indicating that the dense disk is crucial for the production of symmetric Galactic bubbles.

GC. Then, beyond 25 kpc the gas is assumed to be isothermal with $T = 10^6$ K and follows the observed density profile of (Tepper-García et al. 2015) out to a radius of 250 kpc.

Fig. 7a shows the comparison between the simulated (top) and observed (bottom) all-sky map in the range 0.6–1.0 keV. In the simulated map, the red arrow at the center represents the direction of the bipolar jets, constantly ejecting at an angle of 45° to the disk normal between 0–1.2 Myr. Fig. 7b displays the simulated X-ray photon count rates as a function of Galactic longitudes (red) in the same energy band as in Fig. 7a cut at various Galactic latitudes (as labelled), compared with the observed profiles (black).

First, as shown in Fig. 4a, the half-width of the outermost bubbles is around 7 kpc, corresponding to an half angular width $\sin^{-1}(7 \text{ kpc}/R_\odot) \sim 122^\circ$, which is as wide as the eROSITA bubbles in the simulated X-ray map (top panel in Fig. 7a). We therefore suggest that the eROSITA bubble shells are a signature of compressed forward shocks that

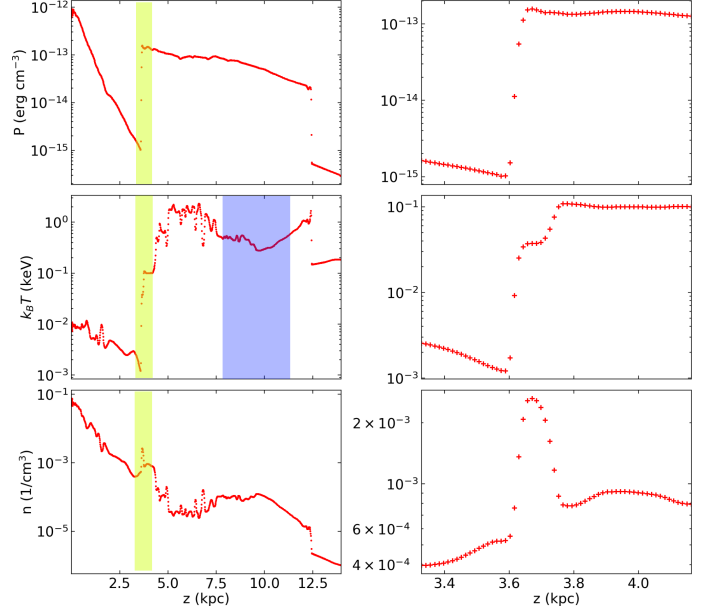


Figure 5. Left: the profiles of pressure (top), temperature (middle), and number density (bottom) along the positive z -axis in Fig. 4. Right: the close-up view of the profiles in the yellow band. The sharp pressure jump at $z = 3.62$ kpc indicates that the innermost bubbles (dashed box in the top panel in Fig. 4a) are an expanding reverse shock.

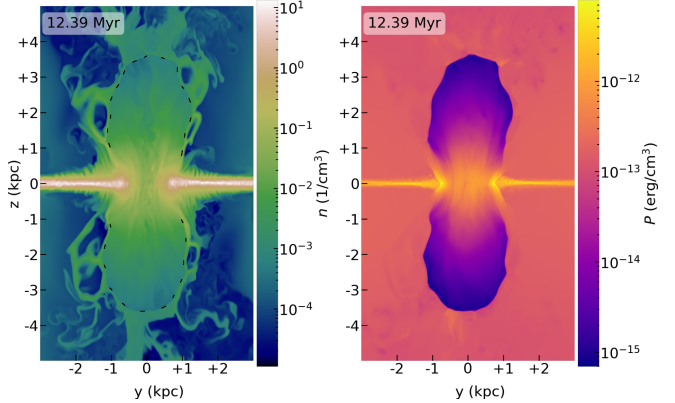


Figure 6. Zoom-in images of the density (left) and pressure (right) slices of the innermost bubbles. The high density upstream of the reverse shock requires an even higher density downstream. Continuing outward, the higher density must match with low density further downstream; thus there exists a dense shell (the turbulent region outside the black dashed line in the left panel).

have been driven into the northern and the southern Galactic halo, as previously proposed by Predehl et al. (2020) and Yang et al. (2022). The broad agreement between simulated and observed X-ray maps hints that the full vertical extent of the eROSITA bubbles can be properly formed by an oblique jet within a thin disk of dense ISM.

Second, we observe that the simulated eROSITA bubbles are not as limb-brightened as the observation. A possibility to enhance the X-ray emission is to include shock-accelerated CRs near the shock, in which CRs could increase the compressibility of the fluid, resulting in the enhanced thermal Bremsstrahlung emissivity that is proportional to density

squared. Also, the disagreement of the northeastern bubble is expected as the North Polar Spur, which is a giant ridge of bright X-ray emission that rises roughly perpendicularly out of the plane of the galaxy, might be a superposition of the GC structure and a remnant of the local supernova (Berkhuijsen et al. 1971; Das et al. 2020; Panopoulou et al. 2021), which is not included in our simulations, whereas analyses based on X-ray data tend to suggest a GC origin (Kataoka et al. 2018b; Sofue 2000; LaRocca et al. 2020).

Third, the innermost bubbles shown in Fig. 4, even though with high column density, are invisible in the simulated X-ray map as the temperature of the innermost bubbles is around 1–10 eV (see the temperature profile in Fig. 5). Consequently, the X-ray emission within the innermost bubbles is severely suppressed by the cutoff $\exp[-h\nu/k_B T]$ in the thermal Bremsstrahlung emissivity. This is the reason why the innermost bubbles are unseen in the X-ray observation.

3.3 Gamma-ray and microwave spectra: constraint on the CRe spectral index

In this section, we obtain the constraint on the CRe spectral index by comparing the simulated gamma-ray and microwave spectra with the observed spectra of the Fermi bubbles (Ackermann et al. 2014) and the microwave haze (Dobler & Finkbeiner 2008), respectively.

We assume the leptonic model for the gamma-ray and microwave emission as previous studies have shown that the bubble and haze spectra can be simultaneously produced by the same population of CRe (Su et al. 2010; Ackermann et al. 2014; Yang et al. 2022). In the leptonic scenario, the gamma-ray and microwave emission come from IC scattering of the ISRF and synchrotron radiation, respectively. Because the evolution of CR spectrum is not modelled in the simulations, we assume that the CRe spectrum is spatially uniform and follows a power-law distribution ranging from 0.5 MeV ($\sim m_e c^2$) to 562.1 GeV. The choice of 562.1 GeV is motivated by the observed cutoff gamma-ray energy shown in Fig. 8 as most of the CRe energy is carried away by the up-scattered photons in the Klein-Nishina limit.

The IC emissivity of the upscattered photons at the energy ϵ_1 is computed for each computational cell in our simulations using the Klein-Nishina IC cross-section (Jones 1968; Blumenthal & Gould 1970) to handle the scattering between ultra-relativistic CRe and photons in the ISRF:

$$\frac{dE}{dtd\epsilon_1 dV} = \frac{3}{4} \sigma_T c \mathbb{C} \epsilon_1 \int_{\epsilon_{\min}}^{\epsilon_{\max}} \frac{n(\epsilon)}{\epsilon} d\epsilon \int_{\gamma_{e,\min}(\epsilon)}^{\gamma_{e,\max}} \gamma_e^{-(p+2)} f(q, \Gamma) d\gamma_e, \quad (7a)$$

$$f(q, \Gamma) =$$

$$2q \ln q + (1 + 2q)(1 - q) + 0.5(1 - q) \frac{(\Gamma q)^2}{1 + \Gamma q}, \quad (7b)$$

$$q = \frac{\epsilon_1 / \gamma_e m_e c^2}{\Gamma (1 - \epsilon_1 / \gamma_e m_e c^2)}, \quad (7c)$$

$$\Gamma = \frac{4\epsilon\gamma_e}{m_e c^2}, \quad (7d)$$

$$\gamma_{e,\min}(\epsilon) = 0.5 \left(\frac{\epsilon_1}{m_e c^2} + \sqrt{\left(\frac{\epsilon_1}{m_e c^2} \right)^2 + \frac{\epsilon_1}{\epsilon}} \right), \quad (7e)$$

where σ_T is the Thomson cross section, c is the speed of light, m_e is the electron mass, $n(\epsilon)$ is the energy distribution of the photon number density in the ISRF given by Porter et al. (2017), γ_e is the Lorentz factor of CRe, and \mathbb{C} and p are the normalization constant and spectral index of the CRe power-law spectrum. $\gamma_{e,\min}(\epsilon)$ is the minimum Lorentz factor of CRe that allows the incident photons to be scattered from energy ϵ to ϵ_1 , and $\gamma_{e,\max}$ is the maximum CRe Lorentz factor in the spectrum. To obtain the simulated IC emissivities, we perform the double integration in Eq. 7 on each cell over the range of the CRe Lorentz factor and the range of incident photon energy between $\epsilon_{\min} = 1.13 \times 10^{-4}$ eV (cosmic microwave background) and $\epsilon_{\max} = 13.59$ eV (optical starlight).

The synchrotron emissivity with an isotropic electron pitch angle distribution is given by Blumenthal & Gould (1970):

$$\frac{dE}{dtd\nu dV} = \frac{4\pi \mathbb{C} e^3 B^{0.5(p+1)}}{m_e c^2} \left(\frac{3e}{4\pi m_e c} \right)^{0.5(p-1)} a(p) \nu^{-0.5(p-1)}, \quad (8a)$$

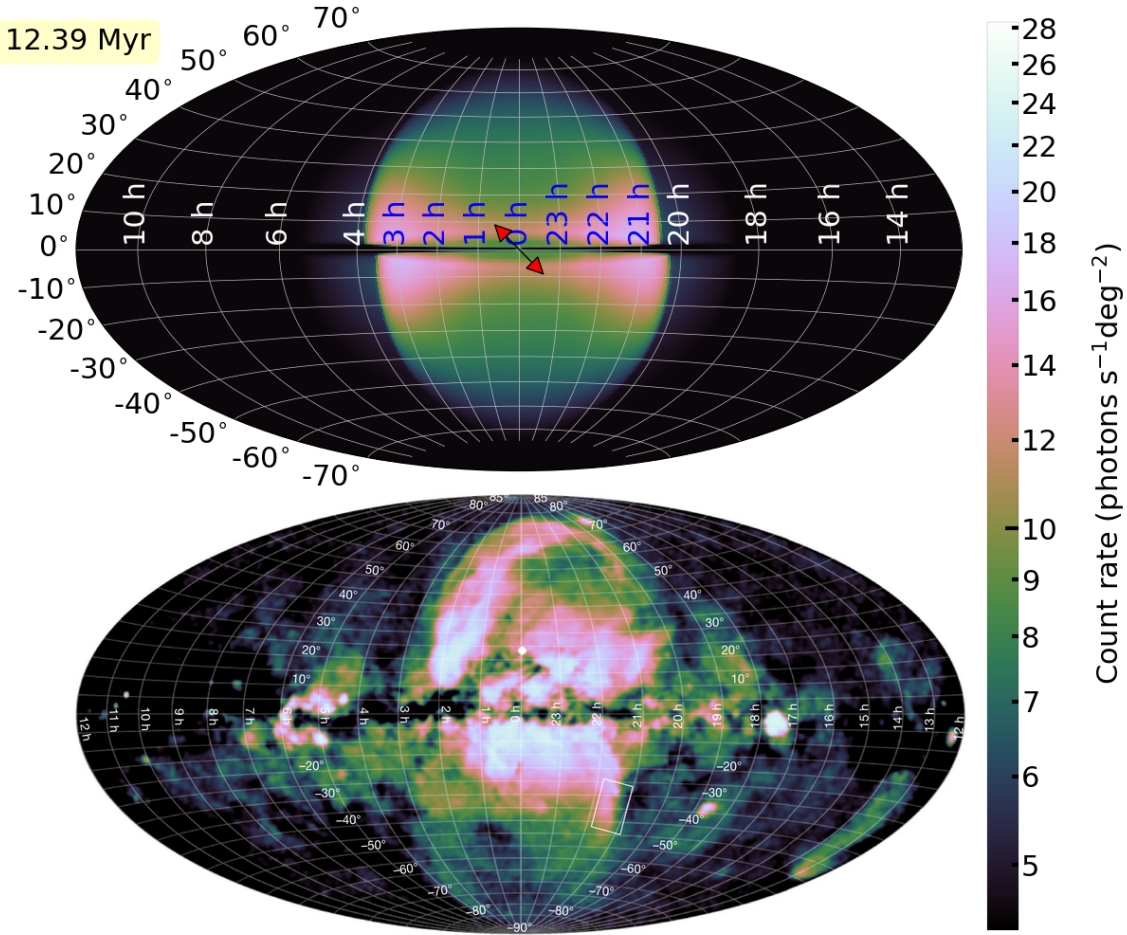
$$a(p) =$$

$$\frac{2^{0.5(p-1)} \sqrt{3} \Gamma [(3p-1)/12] \Gamma [(3p+9)/12] \Gamma [(p+5)/4]}{8\sqrt{\pi}(p+1)\Gamma [(p+7)/4]}, \quad (8b)$$

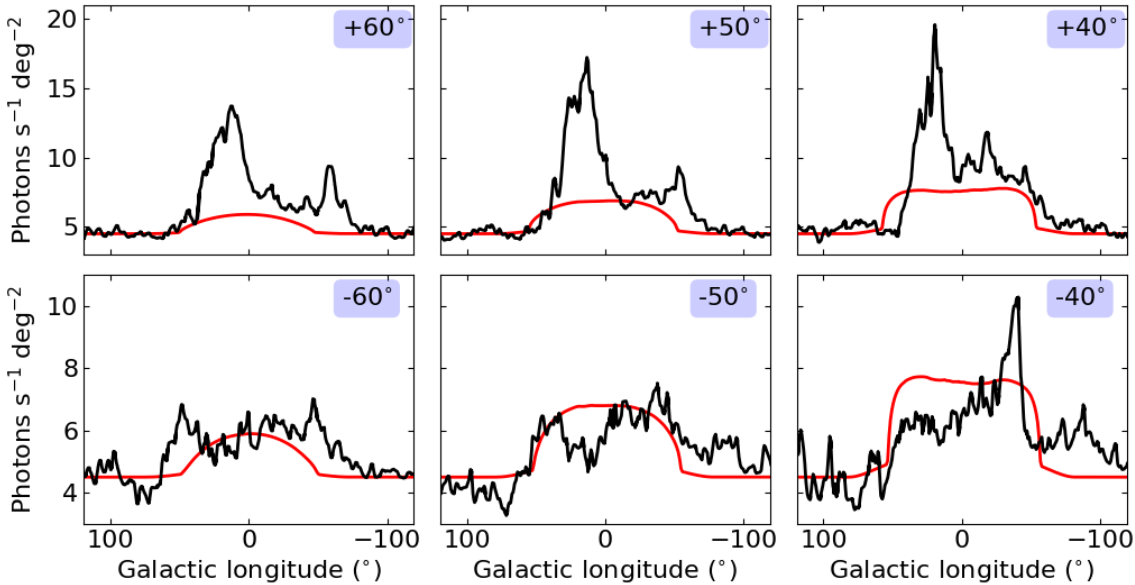
where Γ is the gamma function, and B is the magnetic field strength defined in Eq. 5. For a given longitude and latitude range, the simulated spectra are computed by projecting emissivities as we project X-ray emissivities in Section 3.2, and then we average the spectra over all the sight lines within the region on the sky.

Fig. 8 shows the simulated microwave (left) and gamma-ray (right) spectra averaged over the different patches (shown in the legends) of the sky. The rows from top to bottom show the spectra with different assumptions of the CRe spectral index, 2.2, 2.4 and 2.6. We highlight our findings as follows.

First, we find that, among the three values of the CR spectral indices assumed, a CRe spectral index of 2.4 (the middle row) provides the best fits for both the simulated gamma-ray spectra as well as the microwave spectra. This value is slightly steeper than the best-fit spectral index of ~ 2.17



(a) Simulated (top) and observed (bottom; Predehl et al. 2020) count rate ($\text{photons s}^{-1} \text{deg}^{-2}$) in the 0.6–1.0 keV range. Throughout this paper we show sky maps in Galactic coordinates centered on the Galactic center using a Hammer-Aitoff projection. The red arrow at the center of the top panel depicts the direction of the bipolar jets, constantly ejecting at an angle of 45° to the disk normal for the first 1.2 Myr.



(b) Comparison of the simulated (red) and observed (black; Predehl et al. 2020) one-dimensional photon count-rate profiles in the same energy band as in Fig. 7a, cut at various Galactic latitudes (as labelled).

Figure 7.

found by Ackermann et al. (2014). However, we note that our calculation takes into account the 3D variations of the ISRF, whereas the previous constraint was based on the ISRF at a fixed height of 5 kpc away from the Galactic plane.

Second, the simulated gamma-ray spectra are nearly latitude independent. Note that we have assumed spatially uniform spectrum for the underlying CRe, and hence the simulated gamma-ray spectra at different latitudes mainly reflect how the 3D distribution of the simulated CR number density (see Fig. 10) is projected into different latitude bins. Overall we find good agreement between the simulated and observed spectra (Ackermann et al. 2014); only the simulated spectrum at high latitudes tends to be slightly dimmer than the lower-latitude spectrum because the optical intensity in the ISRF decays with increasing latitudes.

Third, our assumed range for the CRe spectrum (0.5 MeV to 562.1 GeV) produces gamma-ray spectra with a high-energy cutoff around energies 400–500 GeV, consistent with the observed cutoff energy. This is expected since the upscattered high-energy photons ($\epsilon_1 \sim 450$ GeV) mainly arise from the scattering between the relativistic CRe ($\gtrsim 408$ GeV) and optical starlight ($\epsilon \sim 10$ eV). Thus, Eq. 7e can be reduced to $\epsilon_1 \sim \gamma m_e c^2$ in the Klein–Nishina limit (i.e. $\epsilon_1 \epsilon \gg (m_e c^2)^2$), implying most of the CRe energy is carried away by the up-scattered photons.

Finally, the good agreement between the simulated and observed gamma-ray/microwave spectra implies that, in the presence of ISRF and magnetic fields, the emission of the Fermi bubbles and the microwave haze can be produced by the same high-energy electrons via IC scattering and synchrotron radiation, respectively. Our results thus provide further support for the leptonic model as previously suggested (Su et al. 2010; Ackermann et al. 2014; Yang et al. 2013, 2022).

Fig. 9 shows the simulated gamma-ray photon flux with a CRe power-law index 2.4 compared with the observed one in the energy bin 76.8 – 153.6 GeV. As the eROSITA bubbles, one can see that the symmetric *Fermi* bubbles can also be realized by oblique jets. The extent of the simulated gamma-ray bubbles is also comparable to the observed ones. However, we find that the simulated bubble surface is not as smooth as the observed bubbles. The instabilities at the bubble surface may be suppressed by the magnetic draping effect (Lyutikov 2006; Yang et al. 2012) if magnetic fields were included in the simulations. With magnetic draping, the sharp edges of the observed bubbles (Su et al. 2010; Ackermann et al. 2014) could also be explained by anisotropic CR diffusion along field lines (Yang et al. 2013).

The simulated gamma-ray intensity distribution is shown in Fig. 9. Though the overall size of the simulated gamma-ray bubbles is comparable to that of the observed ones, the gamma-ray intensity does not appear to be as uniform as originally found in Su & Finkbeiner (2012). As discussed above, the gamma-ray intensity is slightly higher close to the Galactic plane due to the stronger radiation field at lower latitudes. However, this level of brightness variations appears to be consistent with the later observational data of Ackermann et al. (2014) and Selig et al. (2015), which shows that there are some substructures in the gamma-ray intensity distribution within the bubbles.

For completeness, we show the simulated CR energy den-

sity at 12.39 Myr in Fig. 10. The comparison between Fig. 4 and Fig. 10 shows that the CR pressure is around 5×10^{-15} – 8×10^{-15} erg cm $^{-3}$, bringing the CR-to-gas pressure ratio is 0.1–0.2, similar to 0.18 at the beginning of the simulation. We therefore stress that ignoring the contribution of CR pressure gradient to the momentum of the gas in Eq. 1 is reasonable.

4 DISCUSSION

As a past violent event at the GC must destroy the Central Molecular Zone (CMZ) but the CMZ is currently either in a quasi-steady state or presently increasing (Crocker 2012; Krumholz & Kruijssen 2015; Sormani & Barnes 2019); we conclude that the time since the violent event must be “slightly” shorter than the reconstruction time of CMZ on a timescale of $M_{\text{CMZ}}/\dot{M}_{\text{inflow}}$, where M_{CMZ} is the total mass of molecular gas within $R \sim 300$ pc, and \dot{M}_{inflow} is the gas inflow rate from the Galactic disc at $R \sim 3$ kpc down to the outskirts of the CMZ. Since M_{CMZ} and \dot{M}_{inflow} have been reported to be in the range $2–6 \times 10^7 M_\odot$ (Dahmén et al. 1998; Ferrière et al. 2007) and $0.4–2.7 M_\odot \text{ yr}^{-1}$ (Crocker 2012; Sormani & Barnes 2019), respectively; we estimate that the CMZ formation is about a couple of 10 Myrs, similar to 12 Myr required for our simulated bubbles to reach the desired morphology.

On the other hand, our modeled gamma-ray and microwave spectra assumed that the underlying CRe spectrum is spatially uniform with hard spectral index 2.4; however, the high energy CRe severely suffer from synchrotron and IC losses, during their passage through the magnetic and radiation fields, respectively, within the Galaxy.

The typical synchrotron and IC cooling time scale of high energy (~ 100 GeV) CRe in Milky Way is ~ 1 Myr (Yang & Ruszkowski 2017), ten times shorter than 12 Myr suggested by our simulation. Therefore, the CRe generating the gamma-ray emission would need to be re-accelerated by in-situ acceleration mechanisms such as shocks or turbulence. Since the forward shock is rather far away from the gamma-ray bubbles, re-acceleration is more likely associated with turbulence (Mertsch & Sarkar 2011; Mertsch & Petrosian 2019), possibly in balance with the IC and synchrotron cooling. We will investigate the competition between stochastic acceleration and radiative cooling in future work.

Overall, our results imply that in the oblique-jet scenario, whatever the true re-acceleration and cooling mechanisms are, the CRe spectrum at the present time has to be spatially uniform with a spectral index of 2.4 in order to fit the observed spectra.

5 CONCLUSIONS

In this work, we introduce a thin, dense disk composed of clumpy ISM to stall and thermalize the oblique jets for an outburst event from the central SMBH in the Milky Way Galaxy 12 Myrs ago. We investigate the properties of the Galactic bubbles and the microwave haze using 3D SRHD simulations of CR jet injections from the SMBH assuming the leptonic model. The important findings are summarized as follows.

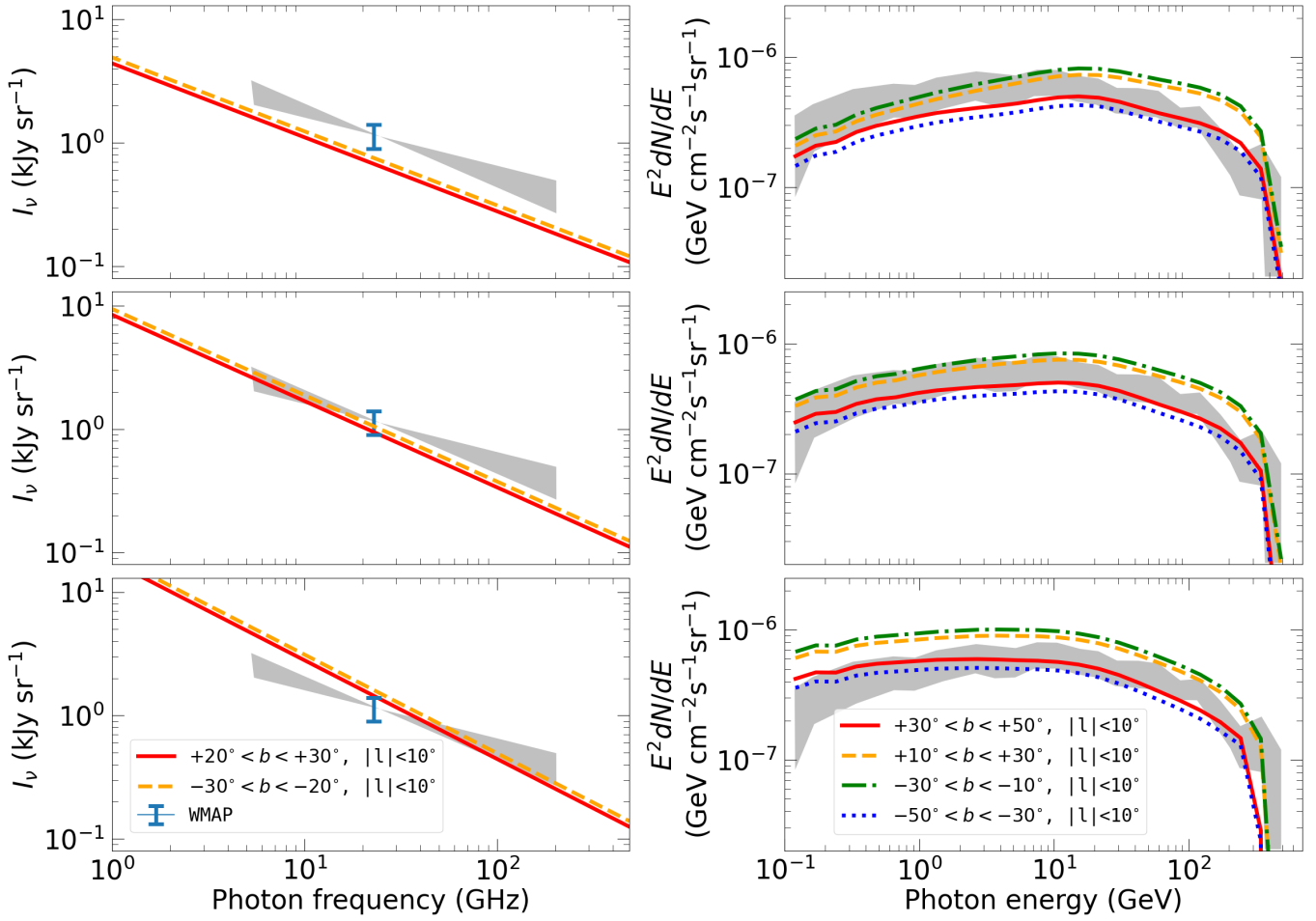


Figure 8. Simulated microwave spectra (colored lines in left) averaged over $20^\circ < |b| < 30^\circ$, $|l| < 10^\circ$. The data point represents the *WMAP* data in the 23 GHz K band and the shaded bow-tie area indicates the range of synchrotron spectral indices allowed for the *WMAP* haze (Dobler & Finkbeiner 2008). Simulated gamma-ray spectra (colored lines in right column) of the *Fermi* bubbles calculated for a longitude range of $|l| < 10^\circ$ for different latitude bins. The gray band represents the observational data of Ackermann et al. (2014). The row from top to bottom shows the microwave (left) and gamma-ray (right) spectra with CRe spectral index 2.2, 2.4 and 2.6, respectively. The CRe cutoff energy is 562.1 GeV in all cases.

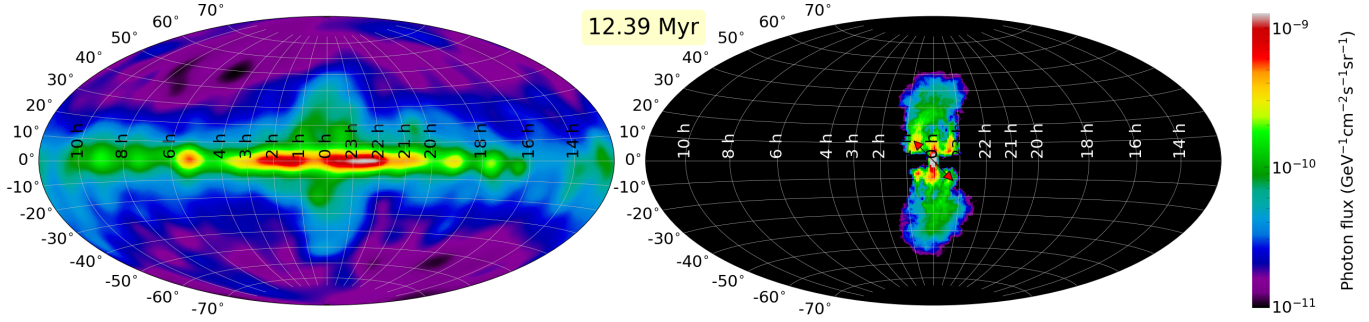


Figure 9. The observed (left; Selig et al. 2015) and simulated (right) photon flux in the energy bin 76.8 – 153.6 GeV. Note that the left panel is the photon flux of the diffuse component reconstructed by the D³PO algorithm (Selig et al. 2015) that analyzes the photon data from the *Fermi* Large Area Telescope (Atwood et al. 2009) and removes the contribution from point-like component. The red arrow at the center of the right panel depicts the direction of the bipolar jet, constantly ejecting at an angle of 45° to the disk normal in 1.2 Myr.

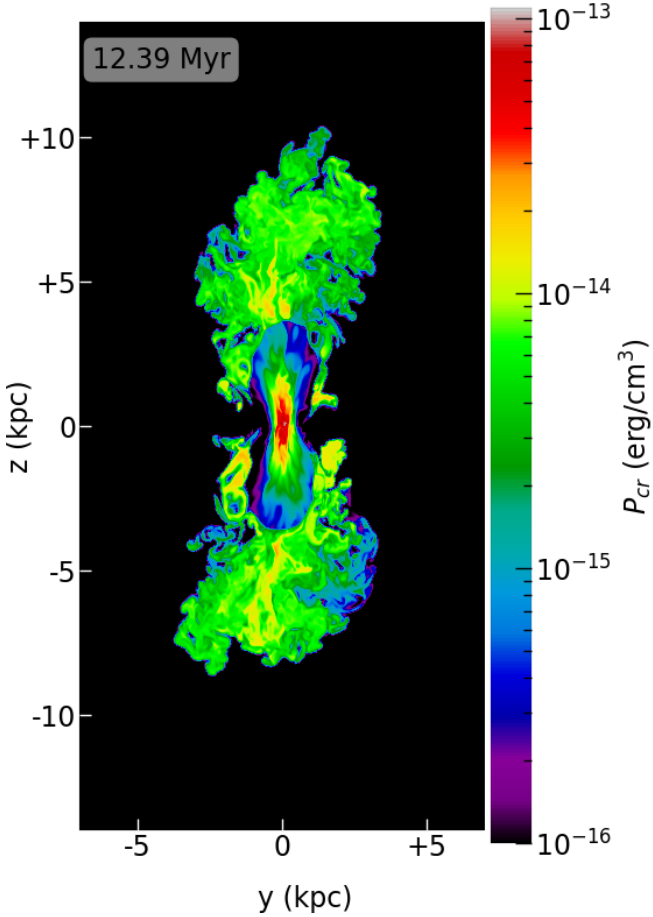


Figure 10. The CR pressure slice passing through the jet source at 12.39 Myr. Comparison between gas pressure (Fig. 4) and cosmic ray pressure shows that the CR pressure is around $5 \times 10^{-15} - 8 \times 10^{-15}$ erg/cm³, bringing the CR-to-gas pressure ratio is 0.1–0.2, similar to 0.18 at the beginning of the simulation. We therefore stress that ignoring the contribution of CR pressure gradient to the momentum of the gas in Eq. 1 is reasonable.

- The development of the expanding forward-reverse shock pair is always associated with the dense disk. In the absence of the disk, the reverse shock is absent, indicating the inclusion of the disk is critical for forming the innermost bubbles.
- The forward-reverse shock pair heats the turbulent plasma considerably (~ 2 keV). There exists a dense shell immediately downstream of the reverse shock, a situation reminiscent of a supernova shell.
- eROSITA bubbles coincide with the forward shock front originally driven by short-lived bipolar jets for a duration of 1.2 Myr, where the bubbles later significantly expanded into the stratified atmosphere to reach the present 12kpc height. The overall extent of the simulated X-ray bubbles is comparable to that of the eROSITA bubbles, though not as limb-brightened. Future models including shock-accelerated CRs may help to resolve this issue by increasing the compressibility of the fluid and enhancing the thermal Bremsstrahlung emissivity at the edge of the X-ray bubbles.
- Downstream of the reverse shock is filled with hot (~ 2 keV) and highly turbulent plasma brought from the disk. The interface between the downstream materials of reverse and forward shocks lies a contact discontinuity, which defines

the edge of the Fermi bubble. The surface of the simulated bubbles is not as smooth as the observed ones; inclusion of magnetic fields in the future may help suppress the instabilities at the bubble surface due to the magnetic draping effect.

- Assuming a power-law CRe energy spectrum ranging from 0.5 MeV to 560 GeV, where the spectrum is space-independent, we showed that the observed gamma-ray and microwave spectra can simultaneously reproduced. The best-fit CRe power-law index is found to be 2.4.

- The elapsed time of 12 Myr is required for the simulated bubbles to reach the desired morphology. This time scale is appropriate for the observed Central Molecular Zone, 200 pc in radius surrounding the GC, to form. However, it is 10 times longer than the typical synchrotron and IC cooling time scale of high energy (~ 100 GeV) CRe. Thus, re-acceleration of CRe by shocks or turbulence must be considered in this model. Since the forward shock is rather far away from the gamma-ray bubbles, stochastic acceleration of CRs by turbulence appears to be more plausible. We will investigate the competition between stochastic acceleration and radiative cooling in a future work.

- The Galactic bubbles are observed nearly symmetric about the Galactic plane albeit the bipolar jets are oblique with respect to the disk normal. We showed that inclusion of the dense ISM disk (regardless of its clumpiness) is an essential ingredient for producing the symmetric Galactic bubbles when the jets are oblique. The broad agreement between the simulated and observed multi-wavelength features demonstrates that oblique failed jets are a plausible scenario for the formation of the Galactic bubbles, which relieve the caveat of earlier jet models where jets need to be vertical.

6 ACKNOWLEDGEMENTS

The authors thank Mateusz Ruszkowski and Ellen G. Zweibel for insightful comments. We thank Henry Zovaro for discussions about the innermost bubbles during the final stages of this work. We thank Peter Predehl for providing the range of observed X-ray intensity in Fig. 7a. We further thank Chen Chun-Yen provides the code module solving the cosmic ray convection equation. A part of the simulations are performed and analyzed using computing resources operated by the National Center for High-Performance Computing (NCHC). HYKY acknowledges support from Yushan Scholar Program of the Ministry of Education of Taiwan and Ministry of Science and Technology of Taiwan (MOST 109-2112-M-007-037-MY3). HS acknowledges funding support from the Jade Mountain Young Scholar Award No. NTU-109V0201, sponsored by the Ministry of Education, Taiwan. This research is partially supported by the Ministry of Science and Technology of Taiwan (MOST) under grants MOST 107-2119-M-002-036-MY3 and MOST 108-2112-M-002-023-MY3, and the NTU Core Consortium project under grants NTU-CC-108L893401 and NTU-CC-108L893402.

DATA AVAILABILITY

The data underlying this article are available in the article and in its online supplementary material.

REFERENCES

- Ackermann M., et al., 2014, *The Astrophysical Journal*, 793, 64
- Ade P. A. R., et al., 2013, *Astronomy & Astrophysics*, 554, A139
- Arnaud K. A., 1996, in Jacoby G. H., Barnes J., eds, Astronomical Society of the Pacific Conference Series Vol. 101, Astronomical Data Analysis Software and Systems V. p. 17
- Atwood W. B., et al., 2009, *The Astrophysical Journal*, 697, 1071
- Berkhuijsen E. M., Haslam C., Salter C., 1971, *Astronomy and Astrophysics*, 14, 252
- Blitz L., Robishaw T., 2000,] 10.1086/309457, 541, 675
- Blumenthal G. R., Gould R. J., 1970, *Reviews of Modern Physics*, 42, 237
- Carretti E., et al., 2013, *Nature*, 493, 66
- Cecil G., Bland-Hawthorn J., Veilleux S., Filippenko A. V., 2001, *The Astrophysical Journal*, 555, 338
- Crocker R. M., 2012, *Monthly Notices of the Royal Astronomical Society*, 423, 3512
- Crocker R. M., Aharonian F., 2011, *Phys. Rev. Lett.*, 106, 101102
- Crocker R. M., Jones D. I., Melia F., Ott J., Protheroe R. J., 2010, *Nature*, 463, 65
- Crocker R. M., Bicknell G. V., Taylor A. M., Carretti E., 2015, *ApJ*, 808, 107
- Dahmén G., et al., 1998, <http://dx.doi.org/10.1051/aas:1997389>
- Das K. K., Zucker C., Speagle J. S., Goodman A., Green G. M., Alves J., 2020, *Monthly Notices of the Royal Astronomical Society*, 498, 5863
- Dobler G., Finkbeiner D. P., 2008, *The Astrophysical Journal*, 680, 1222
- Dopita M. A., et al., 2015, *The Astrophysical Journal Supplement Series*, 217, 12
- Federrath C., Roman-Duval J., Klessen R. S., Schmidt W., Low M.-M. M., 2010, *Astronomy and Astrophysics*, 512, A81
- Ferrière K. M., 2001, *Rev. Mod. Phys.*, 73, 1031
- Ferrière K., Gillard W., Jean P., 2007, *Astronomy and Astrophysics*, 467, 611
- Gallimore J. F., Axon D. J., O'Dea C. P., Baum S. A., Pedlar A., 2006, *The Astronomical Journal*, 132, 546
- Grcevich J., Putman M. E., 2009,] 10.1088/0004-637x/696/1/385, 696, 385
- Guo F., Mathews W. G., 2012, *The Astrophysical Journal*, 756, 181
- Guo F., Mathews W. G., Dobler G., Oh S. P., 2012, *ApJ*, 756, 182
- Heywood I., et al., 2019, *Nature*, 573, 235
- Johnston K. V., Spergel D. N., Hernquist L., 1995, *The Astrophysical Journal*, 451, 598
- Jones F. C., 1968, *Physical Review*, 167, 1159
- Kaastra J. S., Mewe R., 1993, *A&AS*, 97, 443
- Kataoka J., Sofue Y., Inoue Y., Akita M., Nakashima S., Totani T., 2018a, *Galaxies*, 6, 27
- Kataoka J., Sofue Y., Inoue Y., Akita M., Nakashima S., Totani T., 2018b, *Galaxies*, 6, 27
- Krumholz M. R., Kruijssen J. M. D., 2015, *Monthly Notices of the Royal Astronomical Society*, 453, 739
- LaRocca D. M., Kaaret P., Kuntz K., Hodges-Kluck E., Zajczyk A., Bluem J., Ringuette R., Jahoda K. M., 2020, *The Astrophysical Journal*, 904, 54
- Lewis G. M., Austin P. H., 2002, 1th Conference on Atmospheric Radiation
- Li Z., Morris M. R., Baganoff F. K., 2013, *ApJ*, 779, 154
- Liedahl D. A., Osterheld A. L., Goldstein W. H., 1995, *ApJ*, 438, L115
- Lyutikov M., 2006, *Monthly Notices of the Royal Astronomical Society*, 367, 1594
- Mathews W. G., 1971, *ApJ*, 165, 147
- Mertsch P., Petrosian V., 2019, *Astronomy & Astrophysics*, 622, A203
- Mertsch P., Sarkar S., 2011, *Phys. Rev. Lett.*, 107, 091101
- Mewe R., Gronenschield E. H. B. M., van den Oord G. H. J., 1985, *A&AS*, 62, 197
- Miller M. J., Bregman J. N., 2013, *The Astrophysical Journal*, 770, 118
- Miller M. J., Bregman J. N., 2016, *The Astrophysical Journal*, 829, 9
- Morganti R., Oosterloo T., Oonk J. B. R., Frieswijk W., Tadhunter C., 2015, *Astronomy & Astrophysics*, 580, A1
- Mou G., Yuan F., Bu D., Sun M., Su M., 2014, *ApJ*, 790, 109
- Narayanan S. A., Slatyer T. R., 2017, *Monthly Notices of the Royal Astronomical Society*, 468, 3051
- Panopoulou G. V., Dickinson C., Readhead A. C. S., Pearson T. J., Peel M. W., 2021, *The Astrophysical Journal*, 922, 210
- Ponti G., et al., 2019, *Nature*, 567, 347
- Porter T. A., Jóhannesson G., Moskalenko I. V., 2017, *The Astrophysical Journal*, 846, 67
- Predehl P., et al., 2020, *Nature*, 588, 227
- Predehl P., et al., 2021, *Astronomy & Astrophysics*, 647, A1
- Sarkar K. C., Nath B. B., Sharma P., 2015, *Monthly Notices of the Royal Astronomical Society*, 453, 3828
- Schive H.-Y., Tsai Y.-C., Chiueh T., 2010, *The Astrophysical Journal Supplement Series*, 186, 457
- Schive H.-Y., ZuHone J. A., Goldbaum N. J., Turk M. J., Gaspari M., Cheng C.-Y., 2018, *Monthly Notices of the Royal Astronomical Society*, 481, 4815
- Selig M., Vacca V., Oppermann N., Enßlin T. A., 2015, *Astronomy & Astrophysics*, 581, A126
- Sofue Y., 2000, *The Astrophysical Journal*, 540, 224
- Sormani M. C., Barnes A. T., 2019, *Monthly Notices of the Royal Astronomical Society*, 484, 1213
- Strong A. W., Moskalenko I. V., Ptuskin V. S., 2007, *Annual Review of Nuclear and Particle Science*, 57, 285
- Su M., Finkbeiner D. P., 2012, *The Astrophysical Journal*, 753, 61
- Su M., Slatyer T. R., Finkbeiner D. P., 2010, *The Astrophysical Journal*, 724, 1044
- Synge J. L., 1957, North-Holland Pub. Co.; Interscience Publishers
- Taub A. H., 1948, *Physical Review*, 74, 328
- Tepper-García T., Bland-Hawthorn J., Sutherland R. S., 2015, *The Astrophysical Journal*, 813, 94
- Tseng P.-H., Schive H.-Y., Chiueh T., 2021, *Monthly Notices of the Royal Astronomical Society*, 504, 3298
- Valenti E., et al., 2018, *A&AS*, 616, A83
- Wagner A. Y., Bicknell G. V., Umemura M., 2012, *The Astrophysical Journal*, 757, 136
- Yang H.-Y. K., Ruszkowski M., 2017, *The Astrophysical Journal*, 850, 2
- Yang H.-Y. K., Ruszkowski M., Ricker P. M., Zweibel E., Lee D., 2012, *The Astrophysical Journal*, 761, 185
- Yang H.-Y. K., Ruszkowski M., Zweibel E., 2013, *Monthly Notices of the Royal Astronomical Society*, 436, 2734
- Yang H.-Y., Ruszkowski M., Zweibel E., 2018, *Galaxies*, 6, 29
- Yang H.-Y. K., Ruszkowski M., Zweibel E. G., 2022, *Nature Astronomy*
- Zhang R., Guo F., 2020, *The Astrophysical Journal*, 894, 117
- Zhu Z., Li Z., Morris M. R., Zhang S., Liu S., 2019, *ApJ*, 875, 44
- Zweibel E. G., 2013, *Physics of Plasmas*, 20, 055501

APPENDIX A: JETS PARAMETER VARIATIONS

It is instructive to compare the simulation results (Fig. A1) using exactly same parameters except for the density (ρ), temperature ($k_B T$), and four-velocity ($\beta\gamma$) within the jet source. The parameters of jet source, including the fiducial run (C), covered in this appendix are given in Table A1.

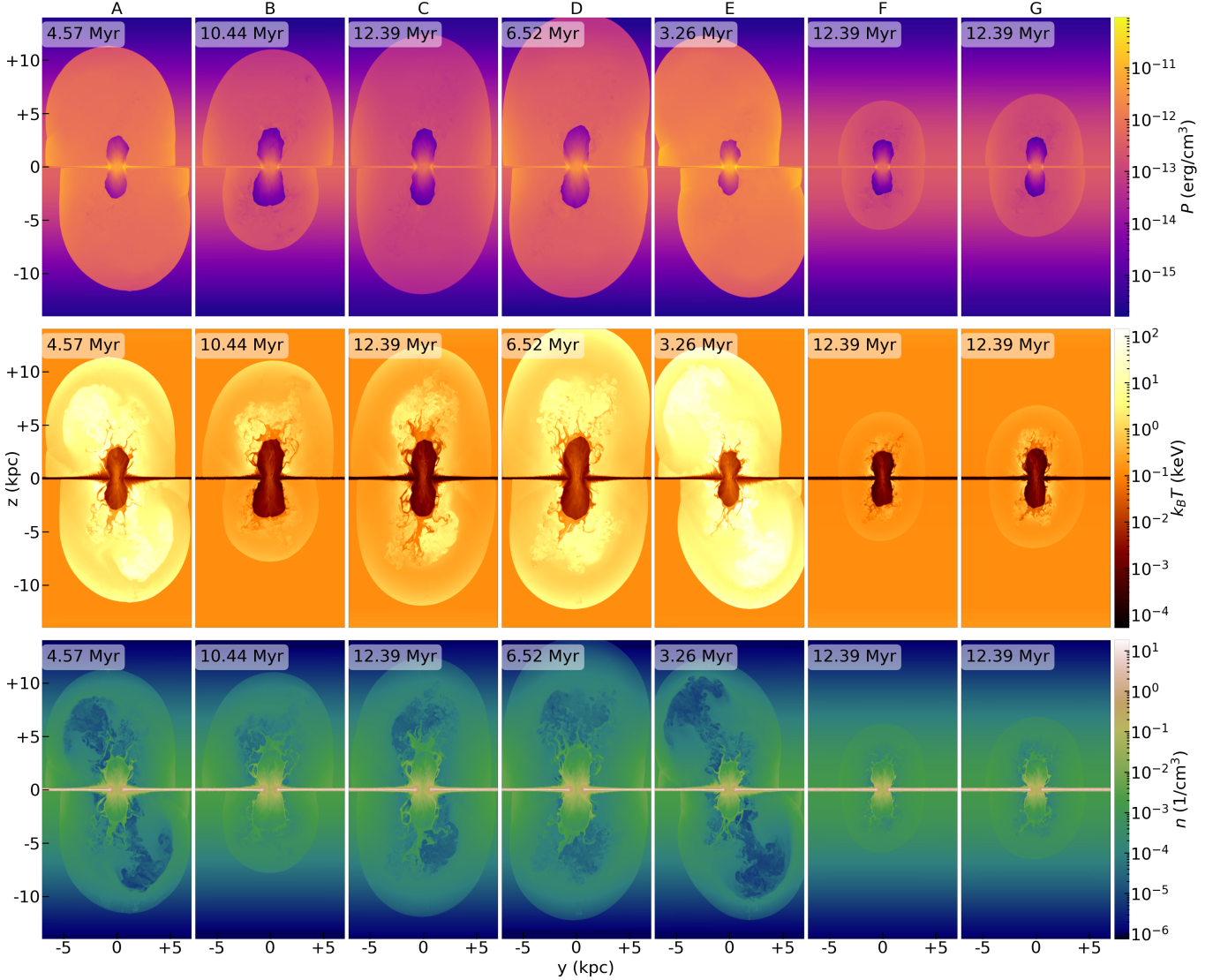
We observe that either higher density (F→C→E) or higher

velocity ($G \rightarrow C \rightarrow A$) of the source can enhance the intensity of the shocks driven into the atmosphere, and makes the post-shock region hotter, as well as leads the bubbles to be more asymmetric about the GC. This is because the denser/faster jets are more likely to break through the thin disk in a short time, so that the jets have insufficient time to interact with the disk to change their orientations and then be vertically elongated by the stratified atmosphere.

Finally, we find that increasing the source temperature ($B \rightarrow C \rightarrow D$) not only improves the symmetry of the bubbles but also increases the temperature inside the bubbles at the present time. This result implies that a high-temperature source helps the jets ablate the clumpy dense gas away and pours into the atmosphere through the intercloud channels of the clumpy disk. In contrast, if source temperature is not high enough, the jets cannot effectively ablate the high-density clouds within 12 Myr, resulting in the formation of asymmetric bubbles (case B).

Table A1. The list of runs showing different injected jet parameters. The fiducial run (C) has been pointed out by an asterisk in the list.

	A	B	C*	D	E	F	G
$k_B T$ (MeV)	1.720	0.034	1.720	86.100	1.720	1.720	1.720
ρ (g/cm ³)	10^{-26}	10^{-26}	10^{-26}	10^{-26}	10^{-25}	10^{-27}	10^{-26}
$\beta\gamma$	1.20	0.60	0.60	0.60	0.60	0.60	0.3

**Figure A1.** Simulation results based on the jets parameters in Table. A1.